Flow Field Analysis of Fully Coupled Computations of a Flexible Wing undergoing Stall Flutter

Casey Fagley[*], Jürgen Seidel[†], Thomas McLaughlin[‡]

Department of Aeronautics, U.S. Air Force Academy, CO 80840, USA

Fully coupled CFD-CSD simulations using HPCMP CREATE[™]-AV Kestrel were performed to compute the dynamic aeroelastic behavior of a torsionally flexible, finite aspect ratio NACA0018 wing. The uncontrolled dynamic instability resulted a very periodic limit cycle oscillation largely governed by the dynamic stall phenomenon. Three-dimensional effects due to the spanwise twist variation produces a localized stalled region which is bound by small interior angles of attack and the wing tip vortex outboard. The flow field at various phases throughout the limit cycle oscillation of the flowfield are shown to characterize the three dimensional flow structures. The coherence and development of a leading edge vortex is reduced due to the three-dimensionality of the problem. In addition to the uncontrolled case, the ability to suppress flutter through momentum addition through a blowing port at 75% span is detailed. By varying the amount of momentum addition added through a slot, varying control authority to suppress the aeroelastic instability is observed. In particular, two flow states are attained for depending on the magnitude of momentum addition.

Nomenclature

A_j	Jet orifice area	q	Structural displacement
C	Damping	s	Laplace variable
C_D	Drag coefficient	$\hat{U}$	Jet velocity vector
C_L	Lift coefficient	U_∞	Freestream velocity
C_μ	Momentum coefficient	U_j	Jet velocity magnitude
K	Stiffness	R	Aspect ratio
M	Mass	ρ	Density
$\hat{n}$	Normal vector		

I.   Introduction

Aeroelasticity is a very well studied field investigating the interaction of structural dynamics and aerodynamics. These aeroelastic interactions can be represented by Collars triangle of forces; the transfer of energy between inertial, elastic, and aerodynamic forces produces aeroelastic phenomena. These fluid-structure interactions are prominent design considerations for current air vehicles; for instance, at certain operating conditions (i.e. Mach, altitude, weight, fuel levels, etc.) aeroelastic instabilities may be detrimental to the integrity of the aircraft structure. Such instabilities are typically identified as flutter, or in the situation of a marginally stable system, a limit cycle oscillation.

Aircraft design needs to maintain a reasonable safety margin from any aeroelastic instability; therefore, a wide variety of methods exist to predict flutter margins.[1–4] Each of these methods aim to identify the true damping of the aerodynamic-structure system, i.e. the flutter boundary, as a function of operating condition (mainly Mach and altitude). Current aircraft designs are pushing these stability margins to achieve lighter and therefore more efficient flight vehicles; thus, the need to understand the flow details associated with these aeroelastic instabilities and to suppress the instability is greater than ever.

The traditional approach to suppressing aeroelastic instabilities is by using control surfaces, i.e. flaps or ailerons, to counteract unsteady aerodynamic loads due to structural displacements. In terms of actuation, most, if not all, active

---

aeroelastic control endeavors utilize a conventional trailing edge flap to alter the aerodynamics. For instance, in the case of the design of the X-56A, a NASA designed Multi-Utility Technology Testbed for flutter suppression techniques, conventional trailing edge flap actuators with a bandwidth of 10 Hz[5] was used. Interestingly, the frequencies associated with the flutter instabilities were on the order of 5-15 Hz.[6]

In addition, sensors such as accelerometers and strain gauges have long been used to instantaneously measure the wing deformation. Clearly, these sensors rely upon the structural deformation for determining the extent of the deformation and for mitigating the aeroelastic phenomena. The bandwidth demand for flutter suppression is a significant problem for the stability and robustness of the control system and, ultimately, leads to the motivation of this work: to employ active flow control to augment the local flow features to suppress aeroelastic instabilities.

Active flow control, which introduces a small amount of energy to the flow (e.g. by blowing fluid into the main flow), allows for direct, local, and instantaneous modification of the flow field. The perturbation of the flow is amplified through a natural fluidic instability which affects the global flow state which allows the control effort to remain small. The bandwidth of the system is equivalent to the convective frequency of the flow.[7] In the past, both passive and active (which includes open- and closed-loop) flow control techniques have been the topic of considerable research (see review articles, e.g. [8],[9]), but upon a survey of the literature, implementation of active closed-loop flow control in real-life applications has largely eluded the research and engineering communities to date.[9] The development of a functioning control system for a range of flow conditions has proven to be a formidable challenge.

The research in this paper utilizes CREATE-AV/Kestrel, a fully coupled computational fluid dynamic (CFD) and computational structural dynamic (CSD) code, to assess aeroelastic phenomena of a flexible, fluttering, rectangular wing. A flow analysis is done which isolates of two and three dimensional flow features. A range of flow states are shown during the limit cycle oscillation and the influence of the flow features on the aeroelastic instability are quantified. Finally, the influence of actuation through a blowing port at 75% span is shown.

II. Setup

Simulations were performed on a fixed, cantilevered NACA0018 wing with aspect ratio of, $\mathcal{R} = 6$. The geometry of the wing consisted of a 0.6 meter span and 0.1 meter chord. The velocity of the simulations were performed at Mach 0.1, which corresponded to a Reynolds number of 160,000. The geometry is shown in Figure 1. A single rectangular blowing slot was integrated 75% span. The slot dimensions are 0.5% by 10% chord. The orientation of the slot was chosen to be 30 ° upward and forward from the 10% chord line. The slot location and geometry is also shown in Fig. 1.

A. Coupled Aeroelastic CFD

The Department of Defense High Performance Computing Modernization Program (DoD HPCMP)*Kestrel* software suite was employed for the simulations in this research. The underlying program structure is based upon an event based model, where the various components in the simulation subscribe to and trigger events. This architecture allows for great flexibility of simulations without sacrificing performance and simplifies the development of extensions such as a flow control component.[10–13]

Figure 1. Wing geometry and blowing slot location.

The CFD solver, *Kestrel* v6.0 is second order in space and time and features a number of turbulence models, including Delayed Detached Eddy Simulations (DDES) using the Spalart-Allmaras turbulence model. Currently, the code allows for fully coupled fluid-structure interaction simulations using a second order modal solver with beam, infinite-plate, and thin-plate spline interpolation. In addition, using sliding interfaces, moving control surfaces, and externally controlled boundary conditions can be simulated. Finally, rigid body motion, including full 6 degree-of-freedom (DOF) capabilities, is included. It should be noted that all these
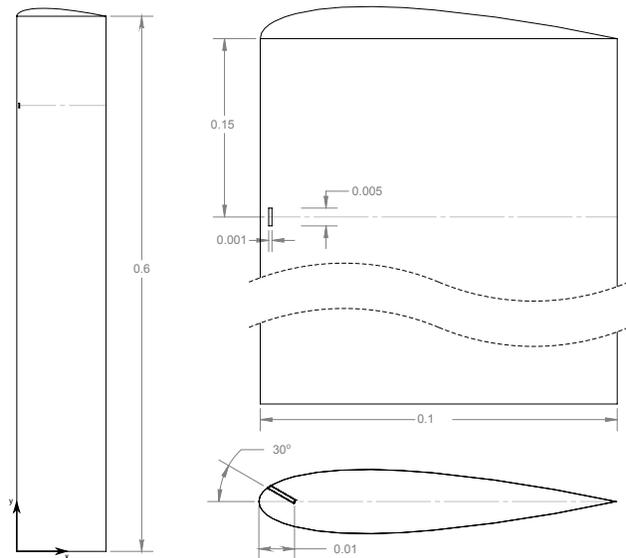
American Institute of Aeronautics and Astronautics

capabilities can be utilized in conjunction, i.e. a 6DOF simulation of a flexible aircraft with moving control surfaces is possible.

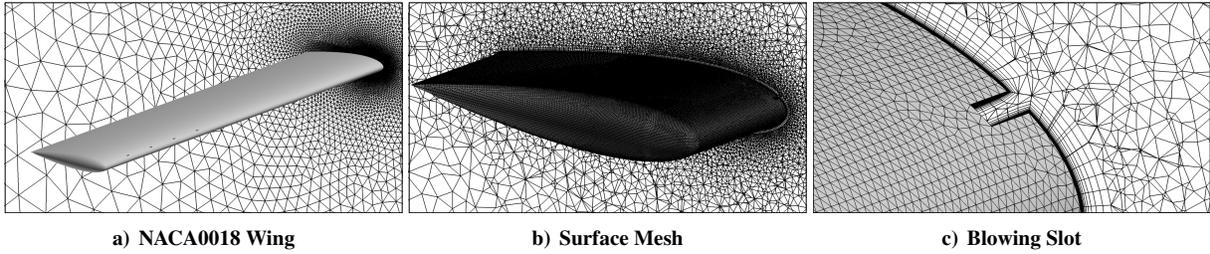a) NACA0018 Wing   b) Surface Mesh   c) Blowing Slot

Figure 2. 20.3 million cell grid of the finite aspect ratio NACA0018 wing.

B. Structural Model

For the implementation of fluid-structure interaction a modal structural model of the geometry is necessary. For the basic problem with a linear elastic material, obeying Hooke's Law, the system of equations to be analyzed is a second order ordinary differential equation describing a mass-spring-damping system. This system is given by

$$[Ms^2 + Cs + K]q = F, \tag{1}$$

where M is the mass matrix, C is the damping matrix, K is the stiffness matrix, q is the displacement, s is the Laplace variable, and F is the forcing function. For vibrational analysis, the homogeneous equation with zero damping is typically analyzed. This is given by

$$[Ms^2 + K]q = 0. \tag{2}$$

From this eigenvalue analysis, the dominant spatial mode shapes and frequencies can be computed. The eigen-solution for a scalar system is the quadratic equation

$$\omega^2 = \frac{K}{M}. \tag{3}$$

i.e. the resonant/fundamental frequency is given by $\omega_n = \sqrt{\frac{K}{M}}$. For practical application and implementation to the CFD simulation environment, the geometry must be discretized and a finite element approach must be used to compute the resulting normalized stiffness matrix. The resulting system of equations can be written as

$$\begin{bmatrix} \dot{\mathbf{q}} \\ \ddot{\mathbf{q}} \end{bmatrix} = \begin{bmatrix} 0 & 1 \\ -\frac{K}{M} & -C \end{bmatrix} \begin{bmatrix} \mathbf{q} \\ \dot{\mathbf{q}} \end{bmatrix}, \tag{4}$$

where the eigen analysis will result in the spatial modes and their frequencies. For the purposes of this paper, the material is homogeneous, thus the mass and damping are constants multiplied by the identity of the given spatial discretization dimension. For this analysis, Nastran was used as the FEM solver. Tetrahedral elements were used to discretize the volume of the wing. A total of 10,000 elements were used to define the wing geometry. Initially, a 2-mode model was used to represent the structural dynamics. The modes consisted of spanwise wing bending and torsion. The resulting spatial modes are shown in Fig 3.

The structural parameters (torsional and bending stiffness) of the wing were selected to match an accompanying experiment to obtain a limit cycle oscillation of a traditional flutter instability. The damping and torsional rigidity was estimated through a flutter prediction technique to develop a wing structure which naturally oscillated at a given velocity (Mach number) and altitude (i.e., dynamic pressure).

C. Fluidic Actuation

In the actuated cases, the actuation strength is governed by the mass flow through the source patch at the base of the forcing slot. To normalize this mass flow with the momentum in the flow, the normalized momentum coefficient, C_μ, is defined as

$$C_\mu = \frac{\int_A \rho \hat{U}(\hat{U} \cdot \hat{n})dA_{jet}}{\rho_\infty U_\infty^2 A_{ref}} \tag{5}$$

American Institute of Aeronautics and Astronautics
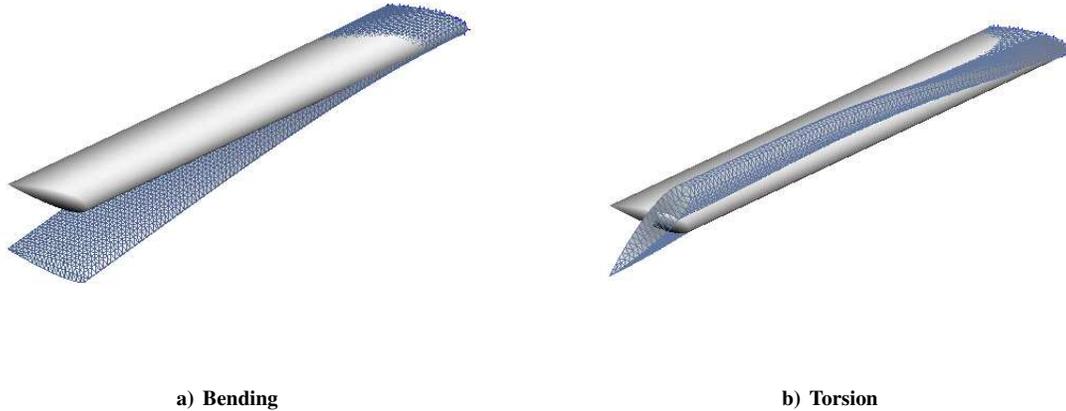
a) **Bending**
b) **Torsion**

Figure 3. Modal structural model containing both bending and torsional modes.

which can be simplified to

$$C_\mu = \frac{U_j^2 A_j}{U_\infty^2 A_{ref}} \tag{6}$$

since the actuation velocity vector is normal to the patch and the flow is incompressible at the jet orifice. The ratio of the jet orifice area to the wing reference area is 1.67×10^{-4}; the chosen velocity ratios and resulting momentum coefficients. Results of the remaining simulations were included to build the model of the influence of forcing on the structural dynamics.

III. Results

A. Unforced simulations

Simulations were performed at an angle of attack of $\alpha = 6°$ to initiate a disturbance in order to self-excite stall flutter. Also, the base angle of attack has been shown to be an important parameter to elicit hard or soft flutter, and also changes the flutter onset velocity.[15] $\alpha = 6°$ was chosen primarily to compare to companion experiments on a cyber-physical wing.[16] The instability at play for this flutter scenario is no longer a dynamic but a static instability which analytically produces rigid body divergence, but due to the nonlinearities in the flow field (i.e. separation, stall, and dynamic stall behavior), the analytically divergent flutter is bounded and a limit cycle oscillation (i.e. stall flutter) is attained.

Stall flutter simulations were restarted from the rigid simulations to minimize startup transients in the flow field. A total of 50,000 time steps were computed which equaled 500 total flow through times. After the initial transient, the flutter oscillation assumed a steady LCO. The LCO was deemed stationary by having a constant minimum and maximum tip angle of attack over the course of 5 cycles. The time histories of the limit cycles are shown in Fig. 4. The angle of attack at the tip of the wing is plotted in Fig. 4a. This shows maximum angles on the order of $20°$ which indicates that stall is indeed occurring. Also, Figure 4b shows the tip displacement (bending) as a function of time. The magnitudes indicate very small bending displacements. This was by design to isolate stall flutter rather than a classical flutter mode. The frequency of the structure was approximately 14.2Hz, and interestingly, the frequency of oscillation of the combined dynamic aeroelastic system was reduced to approximately 12Hz. This trend agrees with experimental measurements of stall flutter[17] where a decrease in torsional frequency is expected after the onset of the aeroelastic instability.

Fig. 5a shows the angle of attack at the tip relative to the to the lift coefficient. The maximum lift coefficient ($C_L = 0.9$) is difficult to compare to traditional aerodynamic analysis due to the angle of twist along the span, but it certainly falls in the ranges of a lift coefficient for a NACA0018 airfoil section. Also, a hysteresis (i.e. the width of LCO) in the tip angle of attack vs. lift coefficient plot is indicative of the aeroelastic system being in an unsteady regime with $k = 0.26$. A reduced frequency of 0 would be the static case while a larger reduced frequency would
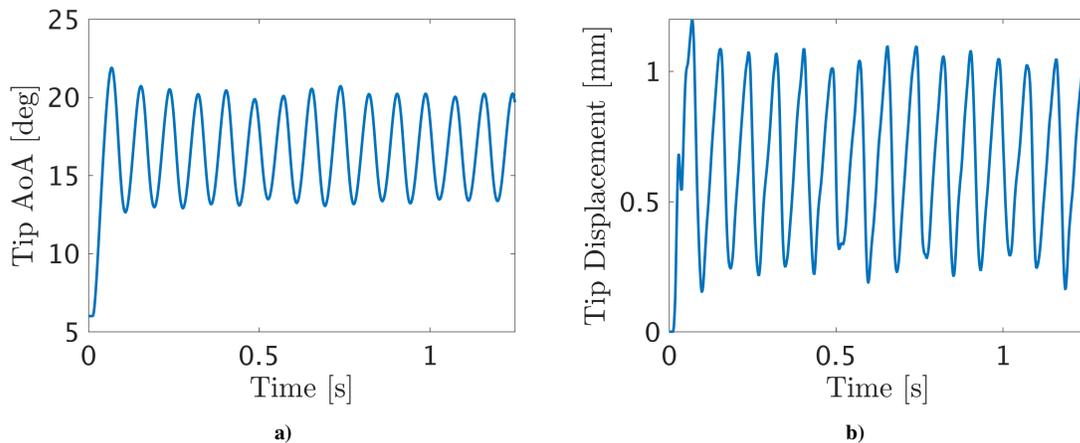
American Institute of Aeronautics and Astronautics

Figure 4. Time histories of limit cycle oscillations for the unforced dynamic aeroelastic simulation.

excite dynamic stall behavior and generate larger lift and larger hysteresis.[18] Furthermore, Figures 5b and 5c also show the LCO behavior for tip angle of attack vs. drag force and tip angle of attack vs. pitching moment, respectively. Similar hysteresis loops are observed in each of the aerodynamic coefficients.
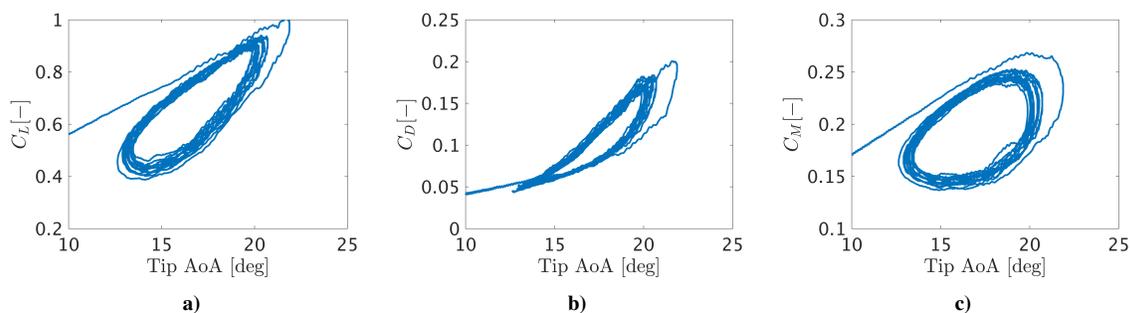

Figure 5. Tip angle of attack versus resulting forces and moments.

To investigate the flow features throughout a period of the LCO, instantaneous snapshots of the flow are shown in Fig. 6. The surface pressure is shown along with the surface streamlines to indicate areas of separated flow.[?] Also, an iso-surface of the scaled Q-criterion is plotted to visualize the structures in the flow. A total of four snapshots are shown to illustrate the changes in the flow field throughout one complete cycle of the LCO. The first image (Fig. 6a) is taken at the mean twist angle of $\theta = 17°$, on the upstroke, and corresponds to the start of the LCO, $t/T = 0$. During the upstroke, it is shown that separation occurs immediately at the slot location. Also, a region of separation propagating forward from the trailing edge. As the pitch cycle reaches it's maximum angle of twist (Fig. 6b), the flow begins to separate at the leading edge which causes a reduction of lift and increase of drag. This separated region now engulfs the region around the slot. During the downstroke, the stalled region propagates outward in the spanwise direction.

Due to the variation of angle of twist across the span, the separated region begins at a local angle of attack larger than $\approx 10°$, which compares favorably with the the static lift curves for the NACA0018 airfoil. At approximately 60 per cent span a large stalled region is observed which extends to 90 per cent span. This indicates that the separated region is bounded on one end by the tip vortex and on the other by small local angles of attack. This flow structure is persistent throughout the LCO, but as the LCO progresses through pitch up, the size of the structures in the stalled region tend to be reduced, potentially due to mechanisms also seen in dynamic stall scenarios. At the peak of the LCO, the flow remains attached at the root while the separation line migrates forward from the trailing edge with increasing spanwise distance. Beyond this time, during pitch down, the flow is reattaching and the LCO repeats itself. During the limit cycle oscillation, the development of a coherent leading edge vortex (LEV) was not observed as in

American Institute of Aeronautics and Astronautics

2D flow fields. It is postulated that the presence of 3D effects, such as the wing tip vortex, the local angle of attack and spanwise pressure gradients disrupt the formation of the LEV.

a) $t/T = 0$, $\alpha = 17°$

b) $t/T = 0.25$, $\alpha = 21°$

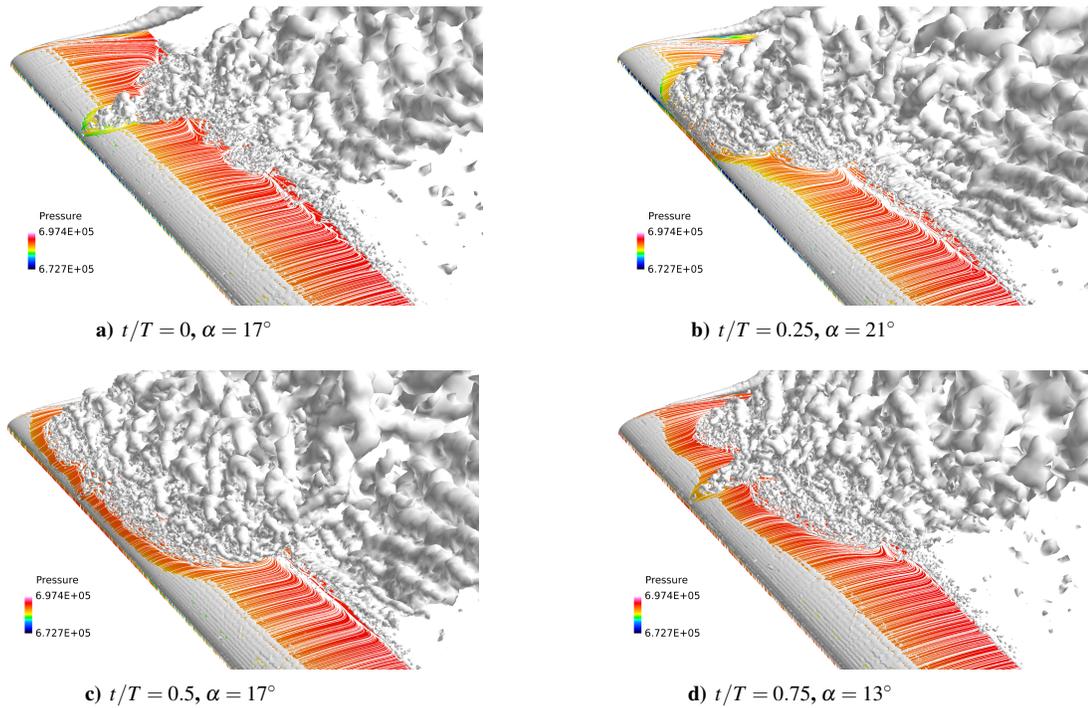c) $t/T = 0.5$, $\alpha = 17°$

d) $t/T = 0.75$, $\alpha = 13°$

Figure 6. Instantaneous snapshots of the flow field throughout the limit cycle oscillation. Initial time, $t = 0$, corresponds to point at which a the mean angle of tip twist is present.

To understand the basic flow features, proper orthogonal decomposition (POD) was used on the pressure in the flow field.[?] Because the mesh is deforming due to the fluid-structure coupling and the flexibility in the wing, the flowfield is observed from a body reference frame and mapped back to the rigid geometry in order to perform such an analysis. POD provides a numerical mechanism to retain the most energetic features of the flow and understand governing flow features during these periodic flow oscillations. The POD modes were computed using singular value decomposition. An isosurface of the corresponding modes are plotted in Fig. 7. The first mode as indicated in Fig. 7a shows the mean flow for the entire limit cycle oscillation. This mode primarily shows the suction peak due to the positive mean angle of attack. Also, the disturbance is shown just aft of the slot indicating a separated region. The second mode (Fig. 7b) shows a large low pressure region where the development of the dynamic stall vortex persists. This is also commensurate with the time history of the mode amplitudes as detailed in Fig. 8. As shown mode 1 is constant. If the time history of mode 2 is compared to the angle of twist, it is shown that the frequencies are similar, but there is a phase lag. This may indicate the development and separation of a dynamic stall vortex.

Mode 3 (Fig. 7c) shows a large mushroom type structure in the separated region. If the temporal behavior of the mode is examined, the frequency also matches that of the angle of twist, and little to no phase delay exists between the two time signals. This indicates that the mode may describe the trailing edge separation behavior which migrates back and forth along the chord due to the angle of twist. Finally, Mode 4 (Fig. 7d) shows a spanwise horseshoe type structure around the separated region. This structure may be due to the roll up of the separated shear layer, and looks similar to a stall cell[19] which has been investigated for rigid, finite aspect ratio wing sections. The temporal behavior shows high frequency content and little to no correlation with the angle of twist which supports the fact that there are multiple timescales at play.

B.   Forced simulations

In the actuated cases, the actuation strength is governed by the momentum flux through the source patch at the base of the forcing slot. This momentum flux is normalized with the momentum flux in the mean flow to provide the
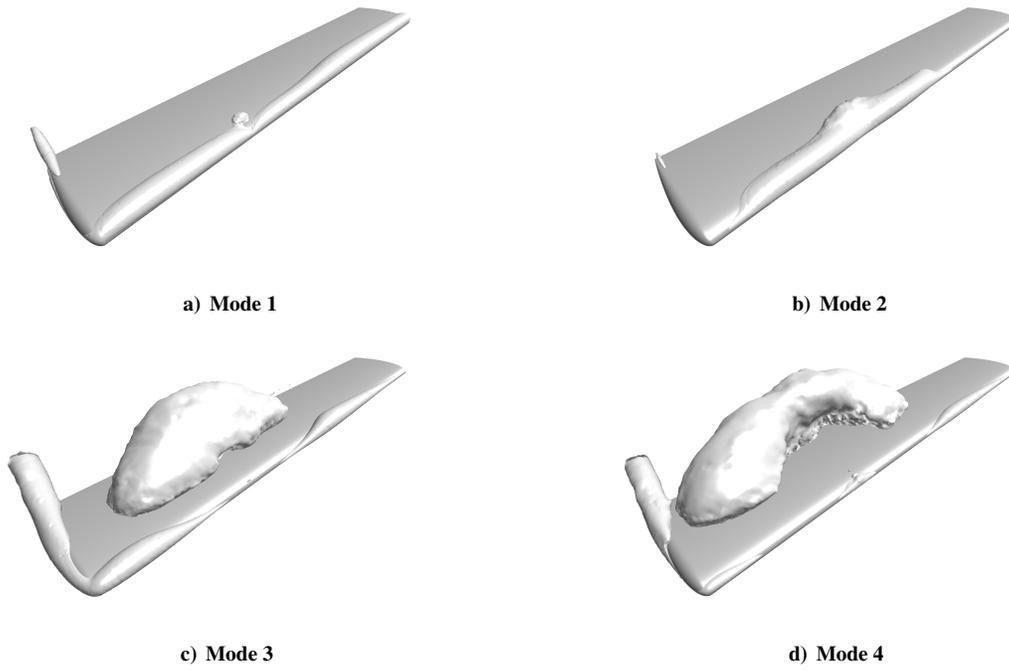
American Institute of Aeronautics and Astronautics

a) Mode 1

b) Mode 2

c) Mode 3

d) Mode 4

Figure 7. First four modes of surface POD of the pressure.
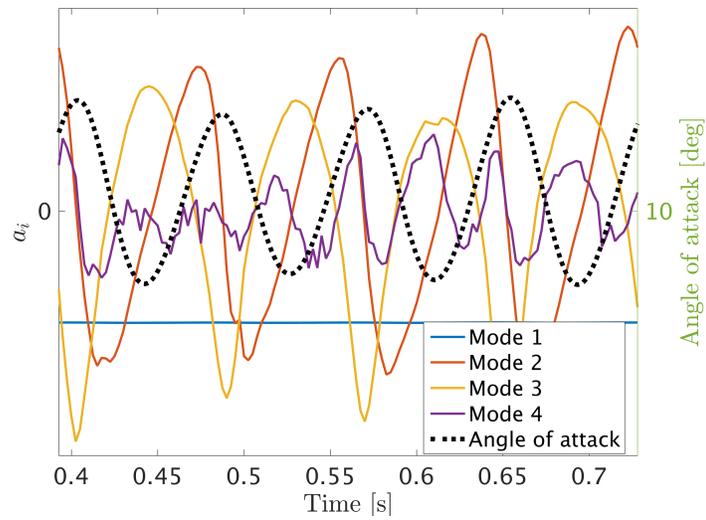
Figure 8. Temporal coefficients of the POD mode set in comparison to the tip angle of twist.

American Institute of Aeronautics and Astronautics

momentum coefficient, C_μ, which is previously defined in Eq **??**. A boundary condition in which the total temperature and pressure was prescribed was applied to the interior of the slot to generate a mass flow through the slot. To determine the outflow velocity as a function of the boundary pressure, a series of simulations with varying specified (constant) pressure on the forcing boundary was performed. An approximate relationship was found by a curve fit as (note that the free stream total pressure is $P_t = 69715$Pa).

$$Ma_j^2 = \frac{1}{2.185 \cdot 10^6} \left(P_{t_{bc}} - 6.925 \cdot 10^5 \right).$$
(7)

A series of constant blowing simulations were performed. The ranges of are detailed in the Table 1. These values were chosen by blowing velocities ratios in comparison with the freestream. They ranged from about 25% to 150% of the freestream velocity. A total of 6 amplitudes were simulated to assess the feasibility of control on the undergoing stall flutter. Each simulation was restarted from the unforced case at $t = 0.5s$ and continued for the remainder of the simulation duration.

Run	1	2	3	4	5	6
Total Pressure	693890	697986	704813	714370	726685	741677
Mach	0.025	0.05	0.075	0.10	0.125	0.15
U_j/U_∞	0.25	0.5	0.75	1.0	1.25	1.5
C_μ	1.77E-5	4.14E-5	7.10E-5	1.04E-4	1.51E-4	2.13E-4

Table 1. Table of parameters for constant blowing

Figure 9 shows the time histories of the tip angle of attack and the bending displacement for two of minimum and maximum constant blowing cases. As shown each of the forcing cases does damp out the LCO. The transient of the larger blowing case is shorter than the transient of the smaller blowing case which indicates a range of control authority. The difference of transients to suppress the stall flutter is approximately three periods. Also, Fig. 9b which shows the bending displacement, indicates that the final state at which the wing equilibrates is slightly different for the two blowing cases presented. Figure 9c shows the LCO for the forced cases with the angle of tip twist plotted versus the pitching moment. Clearly, the forcing of the slot suppresses the unsteady fluid-structure interaction and stabilizes the LCO.
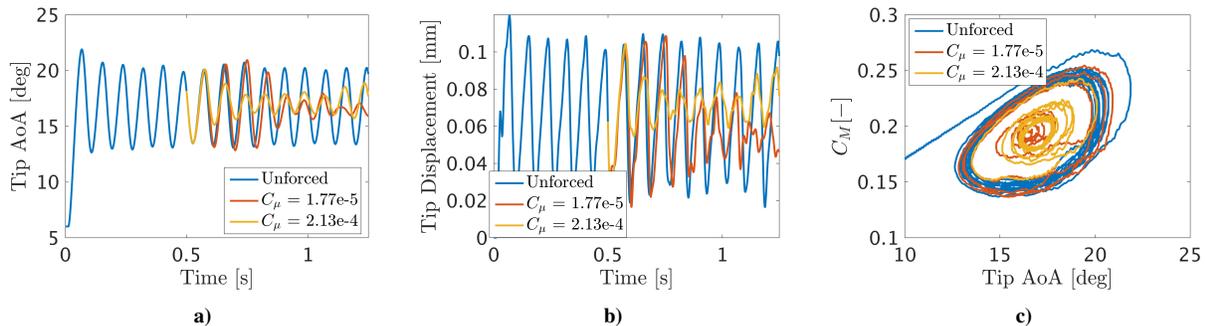

a)   b)   c)

Figure 9. Time histories of limit cycle oscillations for the forced dynamic aeroelastic simulation.

Interestingly, over the range of momentum coefficients investigated, a highly nonlinear effect on the flow can be observed. Figure 10 shows the instantaneous momentum flux from the slot orifice as a function of time. The peaks of the signals indicate a time when low pressure is occurring on the wing surface near the slot causing higher mass flow from the blowing slot. This is what is expected to happen from a physical implementation. Interestingly, these peaks show where the limit cycle oscillation persists as a function of constant mass addition. At large forcing amplitude the LCO is damped very quickly. As the momentum flux is reduced the amount of control authority decreases. Surprisingly, at the smallest momentum coefficient control authority is regained. Upon further investigation, the resulting flow states were vastly difference for the range of momentum coefficients investigated.

To illustrate the change in flow states over the forcing amplitude range, Figure 11 shows a snapshot of the instantaneous flow field for all runs at the final time step. The figures show the surface pressure distribution in color (note that
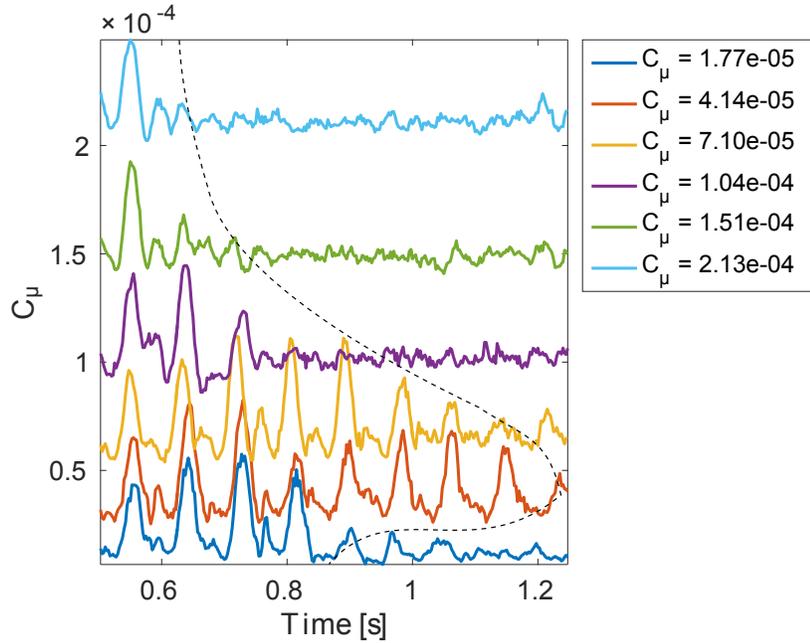
American Institute of Aeronautics and Astronautics

Figure 10. Momentum flux as a function of time for each amplitude of forcing

the pressure is given in $\mathrm{dyn/cm^2}$), surface streamlines in white, and an isosurface of the scaled Q-criterion (Q=0.1) to identify flow structures. When low amplitude forcing is applied ($C_\mu = 1.77e-5$, Fig. 11a), the vortical structures created by the forcing slot push the stalled region outboard toward the wing tip vortex. For the largest forcing amplitude (Fig. 11b), the stalled region is pushed inboard of the forcing slot.

a) $C_\mu = 1.77e-5$

b) $C_\mu = 2.13e-4$
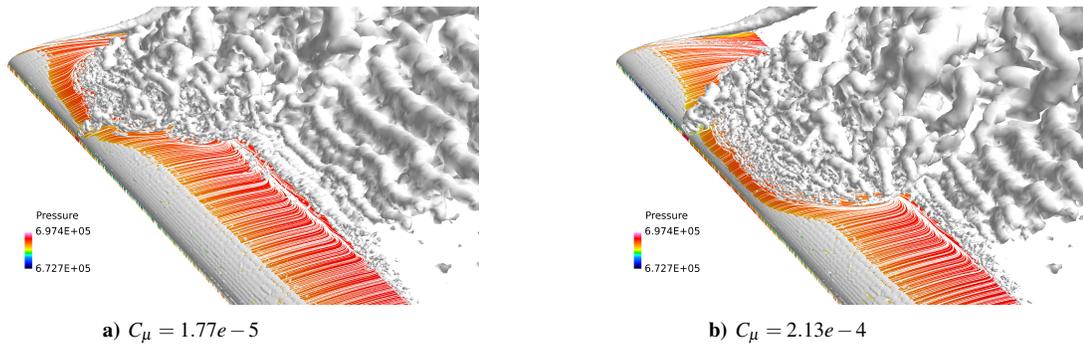
Figure 11. Deformed geometry and isocontours of the Q-criterion (pressure in $\mathrm{dyn/cm^2}$).

IV.   Conclusions and Outlook

Fully coupled, unsteady CFD-CSD simulations of the flow field around an aeroelastically deforming wing were performed. The wing included one actuator port at 75% span through which the amplitude of steady blowing was varied. The unforced simulations showed a periodic LCO in which stall flutter was occurring. The separation region, which was bound by the local inboard angle of attack and the wing tip vortex, migrated from the trailing to leading edge. Three dimensionality and slot geometry broke up the coherence of any observable LEV. Simulations with constant blowing amplitude showed that all applied forcing had a pronounced effect on the unsteady structural oscillations. Large blowing amplitudes caused the stalled region to move inboard of the forcing slot. For small forcing amplitudes, the amplitude of the wing twist limit cycle equilibrated, but the final flow state was different. The stalled region was

now pushed outboard of the slot.

Acknowledgments

References

[1] Hassig, H. J., "An approximate true damping solution of the flutter equation by determinant iteration." *J. Aircraft*, Vol. 8, No. 11, 1971, pp. 885–889.

[2] Chen, Y., Scarborough, D., Liang, S., and Aung, K., "Manipulating Pattern Factor Using Synthetic Jet Actuators," *AIAA Paper 2000-1023*, 2000.

[3] Ju, Q. and Qin, S., "New Improved g Method for Flutter Solution," *J. Aircraft*, Vol. 46, No. 6, 2009, pp. 2184–2186.

[4] Dowell, E. H. and Hall, K. C., "Modeling of Fluid-Structure Interaction," *Ann. Rev. Fluid Mech.*, Vol. 33, 2001, pp. 445–490.

[5] Beranek, J., Nicolai, L., Buonanno, M., Burnett, E., Atkinson, C., Holm-Hansen, B., and Flick, P., "Conceptual Design of a Multi-utility Aeroelastic Demonstrator," *AIAA Paper 2010-9350*, 2010.

[6] Ryan, J. J., Bosworth, J. T., Burken, J. J., and Suh, P. M., "Current and Future Research in Active Control of Lightweight, Flexible Structures Using the X-56 Aircraft," *AIAA Paper 2014-0597*, 2014.

[7] Fagley, C., Porter, C., and McLaughlin, T., "Predictive Flow Control to Minimize Convective Time Delays," *AIAA Paper 2013-5016*, 2013.

[8] Thomas, R. H., Choudhari, M. M., and Joslin, R. D., "Flow and Noise Control: Review and Assessment of Future Directions," Tech. rep., NASA TM-2002-211631, 2002.

[9] Cattafesta, L. N. and Sheplak, M., "Actuators for Active Flow Control," *Ann. Rev. Fluid Mech.*, Vol. 43, 2011, pp. 247–272.

[10] Morton, S. A., McDaniel, D. R., Sears, D. R., Tillman, B., and Tuckey, T. R., "Kestrel A Fixed Wing Virtual Aircraft Product of the CREATE Program," *AIAA Paper 2009-0338*, 2009.

[11] Morton, S. A., McDaniel, D. R., Sears, D. A., Tillmann, B., and Tuckey, T. R., "Rigid, Maneuvering, and Aeroelastic Results for Kestrel - A CREATE Simulation Tool," *AIAA Paper 2010-1233*, 2010.

[12] Morton, S. A., Lamberson, S. E., , and McDaniel, D. R., "Static and Dynamic Aeroelastic Simulations Using Kestrel - A CREATE Aircraft Simulation Tool," *AIAA Paper 2012-1800*, 2012.

[13] Dean, J. P., Clifton, J. D., Bodkin, D. J., and Ratcliff, J., "High Resolution CFD Simulations of Maneuvering Aircraft Using the CREATE-AV/Kestrel Solver," *AIAA Paper 2011-1109*, 2011.

[14] McDaniel, D. R., Tuckey, T. R., and Morton, S. A., "Multiple Bodies, Motion, and Mash-Ups: Handling Complex Use-Cases with Kestrel," *AIAA Paper 2014-0415*, 2014.

[15] Razak, N. A., Andrianne, T., and Dimitriadis, G., "Flutter and stall flutter of a rectangular wing in a wind tunnel," *AIAA J.*, Vol. 49, No. 10, 2011, pp. 2258–2271.

[16] Fagley, C., Seidel, J., and McLaughlin, T., "Experimental Investigation of the Aeroelastic Behavior a NACA0018 Cyber-Physical FlexibleWing," *AIAA Paper 2015-2251*, 2015.

[17] Dimitriadis, G. and Li, J., "Bifurcation behavior of airfoil undergoing stall flutter oscillations in low-speed wind tunnel," *AIAA J.*, Vol. 47, No. 11, 2009, pp. 2577–2596.

[18] Ericsson, L. E., "Dynamic Stall of Pitching Airfoils and Delta Wings, Similarities and Differences," *J. Aircraft*, Vol. 36, No. 3, 1999, pp. 603–605.

[19] Rodríguez, D. and Theofilis, V., "On the birth of stall cells on airfoils," *Theoretical and Computational Fluid Dynamics*, Vol. 25, No. 1-4, 2011, pp. 105–117.